International Journal of Heat and Mass Transfer 124 (2018) 920–928

Contents lists available at ScienceDirect

International Journal of Heat and Mass Transfer

journal homepage: www.elsevier.com/locate/ijhmt

Flow structure and heat transfer of a sweeping jet impinging on a flat wall

Tongil Park [a], Kursat Kara [b], Daegyoum Kim [a,*]

[a] Department of Mechanical Engineering, KAIST, Daejeon 34141, Republic of Korea
[b] Department of Aerospace Engineering, Khalifa University, Abu Dhabi 127788, United Arab Emirates

A R T I C L E I N F O

Article history:
Received 19 August 2017
Received in revised form 26 January 2018
Accepted 3 April 2018
Available online 10 April 2018

Keywords:
Sweeping jet
Impinging jet
Heat transfer
Flow visualization
Flow structure

A B S T R A C T

While an impinging jet has been widely investigated because of its remarkable convective heat transfer performance, the impingement of a sweeping jet which undergoes periodic oscillation has drawn little interest. We experimentally examined the heat transfer of a sweeping jet impinging on a flat wall for several Reynolds number and nozzle-to-plate spacings and discovered unsteady flow structure to characterize heat transfer capability. Local Nusselt number on the wall was evaluated by measuring temperature with thermocouples, and a flow was visualized quantitatively using particle image velocimetry. The distribution of the Nusselt number is different from that of a round jet, exhibiting two distinct regions. Near the center of a sweeping jet, a high Nusselt number zone is formed without a noticeable peak commonly observed in a round jet. Away from the central region, the Nusselt number decreases monotonically. The trends of the Nusselt number at the two regions are correlated with the first mode of the flow structure obtained by proper orthogonal decomposition (POD). The boundary of the two regions is a local minimum of the first POD mode near the wall, and the magnitude of the first POD mode is large in the central region of high Nusselt number. It was also found that the distributions of mean lateral velocity and lateral velocity fluctuation were clearly different between the two regions, which implies that both quantities should be considered for the analysis of heat transfer performance.

1. Introduction

An impinging jet, liquid or gas vertically discharged on a solid surface, has received a lot of attention in the past decades due to its compelling characteristics of enhancing heat transfer [1–11]. The impinging jet has been used in various applications including heat treatment of steel, drying of papers, and cooling of gas turbine blades and electric devices [12–15].

The impinging jet has been mainly investigated for a simple configuration, a steady jet with a simple geometry of a nozzle exit. Martin [3] presented an extensive review on the heat and mass transfer of an impinging jet for three standard types: single circular jet, array jet, and slot nozzle jet. In addition, the empirical relationships that account for nozzle geometry, confinement, turbulent intensity, and nozzle-to-plate spacing have been established by many studies [5,6,11,16].

Besides the simple jet types mentioned above, special types of jets have been introduced: synthetic jet, air-assisted jet, and annular jet. A synthetic jet, a quasi-steady jet generated by periodic suction and squirting motions in a cavity, was used to improve cooling efficiency [14,17]. It was reported that an air-assisted jet, a two-phase flow of liquid and gas bubbles, could enhance heat transfer efficiency as well [18]. Terekhov et al. [19] studied the effect of geometric variables of an annular nozzle and found that the annular jet could increase a heat transfer rate, compared to a basic round jet.

Although past studies on impinging jets have suggested many techniques to enhance heat transfer performance, only recently have studies regarding the effect of unsteady oscillating jet flow on heat transfer emerged. Here, we introduce a fluidic oscillator to generate an unsteady oscillating jet, i.e., a sweeping jet. The fluidic oscillator is an apparatus that produces a bi-stable pulsating jet of sweeping motion [20]. The fluidic oscillator can be generally categorized into feedback and feedback-free oscillators [21], and a feedback-type fluidic oscillator was chosen in this study. Fig. 1 depicts the geometry of a fluidic oscillator with two feedback loops. The mechanism generating a sweeping jet is as follows. At start, pressurized flow from the inlet of the apparatus spontaneously adheres to either wall of an interaction zone inside due to the Coanda effect. At the same time, a jet at the exit is deflected to the opposite side (Fig. 1(a)). The attached primary flow of the

* Corresponding author.
E-mail address: daegyoum@kaist.ac.kr (D. Kim).

https://doi.org/10.1016/j.ijheatmasstransfer.2018.04.016
0017-9310/

Nomenclature

A	surface area of the heated plate (m^2)
d	width of the nozzle exit (m)
H	nozzle-to-plate spacing (m)
h	convective heat transfer coefficient (W/m^2 K)
I	current through the heated plate (A)
k	thermal conductivity of air (W/(m K))
k_p	thermal conductivity of the heated plate (W/(m K))
Nu	local Nusselt number, hd/k
$\dot{m}$	mass flow rate drained into the fluidic oscillator (g/s)
q	rate of heat transfer (W)
R	electrical resistance of stainless steel foil (Ω)
Re	Reynolds number, Ud/ν
T_j	temperature of a jet at the nozzle exit (K)
T_s	local temperature of the heated plate (K)
t	thickness of the heated plate (m)
U	mean velocity of a jet at the nozzle exit (m/s)
$\bar{u}$	mean lateral velocity (m/s)
u'_{rms}	root mean square of the lateral velocity fluctuation (m/s)
$\overline{V}$	mean velocity magnitude (m/s)
w	width of the heated plate (m)
x	lateral coordinate (m)
ϵ	emissivity of the heated plate
ν	kinematic viscosity of air (m^2/s)
σ	Stefan-Boltzmann constant (5.670×10^{-8} W/(m^2 K^4))

interaction zone increases the pressure of the feedback loop in the same side (upper loop in Fig. 1(a)). The increase in pressure pushes the primary flow to adhere to the other side and causes the jet at the exit to change its direction (Fig. 1(b)). This process is repeated, leading to an oscillating sweeping jet.

Unsteady sweeping motion is self-sustained by the internal geometry of a fluidic oscillator without any moving element or actuator. The fluidic oscillator, therefore, is a highly durable device to shock and vibration and is not affected by electromagnetic interference [20–22]. Because of these attractive features, the fluidic oscillator has been broadly applied to many fluid engineering fields including separation control of a boundary layer, jet thrust vectoring, cavity noise reduction, and micro-bubble generation [23–27]. Meanwhile, relatively little has been investigated on the application of a sweeping jet to convective heat transfer. Thurman et al. [28] first applied the sweeping jet to heat transfer and evaluated the effect of the jet flow ejected through a hole into a cross flow on film cooling process. They discovered that a sweeping jet makes cooling performance more uniform on the surface than a jet from a spiral hole. The interaction of a sweeping jet flow and a cross flow was numerically investigated with consideration of an inclination angle to a free stream direction and a blowing ratio [29]. Moreover, Hossain et al. [30] conducted both experimental and numerical studies on film cooling performance, using an array of fluidic oscillators, and found that the array shows significant improvement in cooling effectiveness in the lateral direction because of the sweeping motion of the jet. For a jet vertically impinging on a plate, Lundgreen et al. [31] numerically investigated the thermal performance of a sweeping jet when nozzle-to-plate spacing is greater than 3 hydraulic diameters. This study demonstrated that the average Nusselt number for the fluidic oscillator is higher than that of the steady jet at small nozzle-to-plate spacing and that a fluidic oscillator can provide a more uniform heat transfer rate with a higher average Nusselt number.

In this study, we experimentally investigate the flow structure and heat transfer performance of the sweeping jet generated by a fluidic oscillator, which impinges vertically on a flat wall. Although the heat transfer of an impinging sweeping jet was suggested as a novel technique to improve heat transfer performance in the numerical study of Lundgreen et al. [31], relatively large nozzle-to-plate spacing was considered in their study, and the detailed characteristics of the flow structure and their correlation with the trend of heat transfer performance still remain unclear. By varying Reynolds number and nozzle-to-plate spacing which are known as important parameters to determine the performance of an impinging jet, we will examine noticeable characteristics of heat transfer and reveal correlations between unsteady flow structure and heat transfer performance by employing digital particle image velocimetry and temperature measurement with thermocouples.

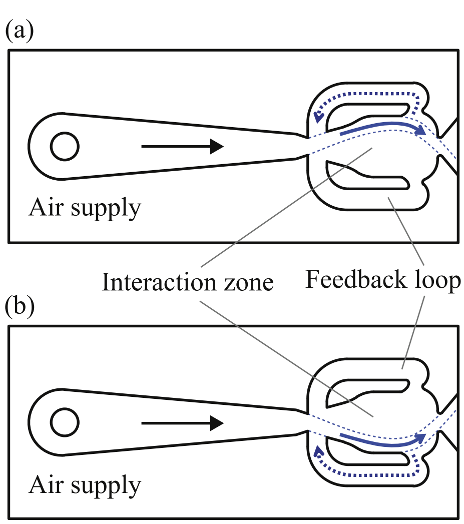

Fig. 1. Geometry of a fluidic oscillator.

2. Experimental setup

A fluidic oscillator design suggested by Stouffer [32] was used to generate a sweeping jet (Fig. 1). The nozzle exit of our fluidic oscillator has a square shape with 6.25 mm width and 6.25 mm height and an exit angle of 100°. The fluidic oscillator was fabricated using a 3D-printer (Ultimaker 2+, Ultimaker Inc.) with Polylactic Acid (PLA) material, and layer thickness in the fabrication process was 140 μm. This layer thickness was much smaller than the length scale of the fluidic oscillator (e.g., nozzle exit width 6.25 mm). Thus, we assumed that jet characteristics were not affected by the surface roughness of the device in this setup. Compressed air was supplied through a regulator integrated with a filter (W4000, CKD Co.) and injected into the fluidic oscillator. The mass flow rate of supplied air was controlled with a mass flow controller with 0.8% accuracy (F-202AV, Bronkhorst High-Tech) installed between the regulator and the fluidic oscillator.

Our experimental study consists of two measurements: convective heat transfer measurement and quantitative flow visualization, which are introduced in Sections 2.1 and 2.2, respectively.

2.1. Experimental setup for heat transfer measurement

To quantify the rate of convective heat transfer, experimental setup was devised as illustrated in Fig. 2. A fluidic oscillator was placed vertically above a heater, and it was connected to a XYZ-axis stage (Namil Optical Instruments Co.) so that it can precisely move with a 0.01 mm increment. A very thin stainless steel foil (ST304, 120 mm $\times$ 5 mm $\times$ 0.04 mm) was used as a heater. Since the maximum difference in the electrical resistivity due to the temperature variance along the foil is 0.58%, we assumed that the heater provided a constant heat flux. A copper bus bar was attached to each end of the foil using an electrically conductive epoxy (CW2400, Chemtronics Inc.), and these bus bars were wired to a DC power supply (MK6003d, MKPOWER Inc.). Resistance of heater and current imposed on the heater were measured to estimate heat flux.

The bottom surface of the foil was covered with a kapton tape of thickness 0.06 mm, which is durable to high temperature and electrically non-conductive. Fourteen thermocouples of K-type were attached to the lower surface of the heater at an equal interval of 2 mm from the center of the heater. After the thermocouples were covered by a kapton tape, to minimize heat loss, the heater was installed on an insulation block (Teflon, thickness 30 mm) with a double-sided tape. Local temperature data of the thermocouples were acquired with a data acquisition board (NI 9212 & cDAQ–9174, National Instruments Co.).

Detailed experimental procedure is as follows. At first, compressed air was supplied into the oscillator, and a downward jet was discharged at the exit of the oscillator. Then, electric power was applied to the heater. A measurement started after 10 min in order to obtain data after a transient phase passed. The temperature of the thermocouples was measured at a sampling rate of 1.8 Hz for 60 s.

The local convective heat transfer coefficient and the corresponding Nusselt number were evaluated by the following equation:

$$Nu_i = \frac{h_i d}{k} = \frac{q_{conv,i} d}{A_i (T_{s,i} - T_j) k}, \tag{1}$$

where $h_i (= q_{conv,i}/A_i(T_{s,i} - T_j))$ is the convective heat transfer coefficient of the flow at a given position of a thermocouple, k is the thermal conductivity of air, and d is the width of the nozzle exit. $q_{conv,i}$ is

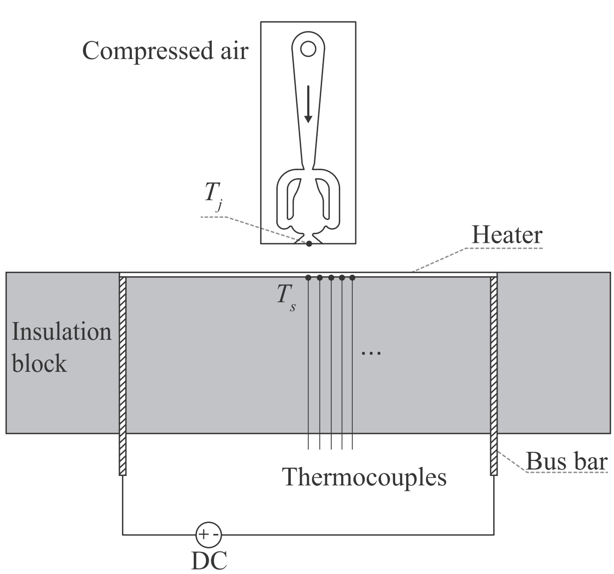

Fig. 2. Experimental setup for heat transfer measurement.

the heat by forced convection of the jet flow. A_i $(= w\Delta x)$ is the surface area of a segment of the heated plate for a thermocouple, and T_s and T_j are the local temperature of the heater and the temperature of the jet at the nozzle exit, respectively. Note that T_s and T_j for Nu obtained in our study are time-averaged values at given positions.

The heat transfer rate by convection $q_{conv,i}$ can be estimated by considering energy balance [33];

$$q_{conv,i} = q_{gen,i} - q_{cond,i} - q_{rad,i} - q_{free,i}, \tag{2}$$

where $q_{gen,i}$ is the rate of electrical energy applied to the foil, $q_{cond,i}$ is conduction heat loss through the foil, $q_{rad,i}$ is radiation heat loss from the top side of the foil, and $q_{free,i}$ is surface heat loss by free convection from the sides of the insulation block. In Eq. (3), the heat generation of the heater was evaluated using the resistance of the foil and the current which was gauged by the power supply.

$$q_{gen,i} = \left(\frac{RI^2}{A}\right) A_i \tag{3}$$

The lateral conduction heat loss was evaluated by solving a one-dimensional energy equation along the foil (Eq. (4)). In most measurement points, the conduction loss in lateral direction remained less than 0.6% of the imposed heat; even maximum conduction loss was just 2.0% in the experiment. Therefore, it is reasonable to assume that the lateral conduction loss is negligible.

$$q_{cond,i} = k_p \left(\frac{\Delta T_{i+1}}{\Delta x_{i+1}} - \frac{\Delta T_i}{\Delta x_i}\right) wt \tag{4}$$

Surface heat transfer by radiation from the top side of the foil is expressed as

$$q_{rad,i} = \epsilon\sigma(T_i^4 - T_\infty^4) A_i, \tag{5}$$

where ϵ is the emissivity of the stainless steel foil, σ is the Stefan-Boltzmann constant. The radiation heat loss is less than 0.8%.

Lastly, in order to evaluate free convection from the block ($q_{free,i}$), we measured the temperature of the vertical sides and horizontal bottom of the block. By applying the correlation between Nusselt number and Rayleigh number, the free convection loss from the block was obtained appropriately [34–36]. The rate of heat transfer imposed in the heater was corrected by the losses caused by radiation from the surface of the foil and free convection from the sides of the block.

For the validation of our experimental setup, we conducted a preliminary experiment with a round jet impinging on a flat wall. The Nusselt numbers obtained by this experiment were compared with the data of Lytle and Webb [6]. Regarding the local Nusselt number at a stagnation point in the range of $6400 \leqslant Re \leqslant 18,400$, the difference between our results and the data of Lytle and Webb [6] was within 10%, which ensured that our setup was able to produce reliable data.

2.2. Experimental setup for flow visualization

Flow visualization experiments were conducted in a glass tank (600 mm $\times$ 450 mm $\times$ 450 mm) with the same fluidic oscillator used for heat transfer measurement (Fig. 3). The fluidic oscillator was mounted in the middle of the tank. One side of the tank was used as an impingement wall.

For planar Particle Image Velocimetry (PIV), seeding particles of 1 μm were generated by an oil droplet generator (Model 9307, TSI Inc.). Compressed air and oil droplets were premixed and supplied into the fluidic oscillator. Mass flow rate was controlled with the mass flow controller. The oil droplets contained in the jet were illuminated by a Nd:YAG laser sheet (Evergreen200, Quantel Inc.) of

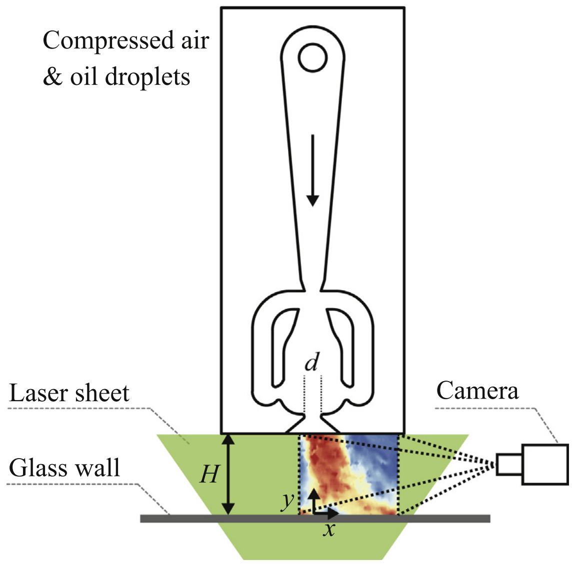

Fig. 3. Experimental setup for flow visualization.

thickness 1 mm on a xy-plane. A CCD camera (GEV-B1620M, Imperx Inc.) captured 2700 image pairs at a rate of 15 pairs per second for each test. A time step between two images of a pair was 1–3 µs. To acquire velocity fields, the captured images were processed with PIVview2C 3.6 (PIVTEC GmbH). For cross correlation of two images in a pair, we used the multi-grid interrogation method; initial interrogation window size was 64×64 pixels and final size was 32×32 pixels. Since the jet from the fluidic oscillator oscillates periodically on the xy-plane, velocity fields were obtained only for a half of the jet, $-0.27 < x/d < 2.72$, between the nozzle exit and the wall (Fig. 3).

From time series of velocity fields, it is difficult to directly figure out the dominant flow structure of an unsteady impinging jet. For the purpose of finding dominant modes which characterize the flow, we employed Proper Orthogonal Decomposition (POD) [37–39]. Here, we briefly introduce the procedure of POD. For detailed mathematical description, refer to Holmes [39]. POD is one of data analysis methods to process a large number of data sets, using orthogonality of modes. A fundamental concept behind POD in fluid mechanics is that the fluctuation of a scalar or vector field, $\boldsymbol{u}(\boldsymbol{x})$, can be approximated as a linear combination of orthonormal bases, $\boldsymbol{\varphi}_j(\boldsymbol{x})$. The present analysis uses the POD based on snapshots (instantaneous flow fields) developed by Sirovich [37], which is appropriate for applying to PIV data with a large number of variables (both u and v-velocity components in all grids).

$$\boldsymbol{u}^k(\boldsymbol{x}) \approx \sum_{j=1}^{N} a_j^k \boldsymbol{\varphi}_j(\boldsymbol{x}). \quad k = 1, \ldots, N \tag{6}$$

$\boldsymbol{u}^k$ is a velocity field at the kth instance, and the number of the bases is equal to the number of snapshots N (the number of instantaneous velocity fields used for POD). The bases (POD modes) can be obtained in a way that minimizes the residue error of the two terms in Eq. (6):

$$\text{Minimize}\left(\left\| \boldsymbol{u}^k(\boldsymbol{x}) - \sum_{j=1}^{N} a_j^k \boldsymbol{\varphi}_j(\boldsymbol{x}) \right\| \right), \tag{7}$$

where $\|\cdot\|$ is a $\mathbf{L}^2$ norm. Eq. (7) is an eigenvalue problem, which leads eigenvalues λ_j $(j = 1, \ldots, N)$ and corresponding orthonormal bases (POD modes) $\boldsymbol{\varphi}_j(\boldsymbol{x})$. The eigenvalue is proportional to the amount of the total kinetic energy of velocity fluctuation contained in the corresponding POD mode; for the larger eigenvalue, the corresponding POD mode is more dominant.

3. Results and discussion

3.1. Heat transfer rate of a sweeping jet

We first investigate the heat transfer performance of a sweeping jet using the experimental setup described in Section 2.1. For a sweeping jet, local Nusselt numbers are evaluated at four Reynolds numbers ($Re = 3600,\ 6400,\ 11{,}000,\ 15{,}300$) and three nozzle-to-plate spacings ($H/d = 1.0, 1.5, 2.0$) (Fig. 4). For the Reynolds number, the mean jet velocity at the exit of the fluidic oscillator U and the width of the exit d were chosen as characteristic velocity and length, respectively: $Re = Ud/\nu$. In all cases considered in this study, maximum local Nusselt number is located in the region of $x/d < 1.0$, the central region of the sweeping jet. See Fig. 2.2 for the definition of a lateral coordinate x/d. Meanwhile, in $x/d > 1.0$, the Nusselt number decreases monotonically with increasing x/d.

The trend of Nu slightly differs between $H/d = 1.0$ and $H/d = 1.5,\ 2.0$ cases. Nu decreases with x/d for all Reynolds numbers of $H/d = 1.0$ and has a local maximum value at the center $x/d = 0$. $H/d = 1.5$ and 2.0 cases tend to exhibit a minor increase in Nu at a certain lateral location off $x/d = 0$, except for the smallest Reynolds number. The magnitude of this minor increase ($\Delta Nu < 1$) is much smaller than the magnitude of Nu in $x/d < 1.0$. In a steady round jet, a noticeable peak of Nu is formed off $x/d = 0$, in addition to at $x/d = 0$, especially in high Reynolds number of $Re > 10^4$ [6]. However, in a sweeping jet, such a noticeable peak is not observed off $x/d = 0$. Instead, a maximum of Nu is established in $x/d < 1.0$. In summary, according to Fig. 4, the region of interest can be divided into two regions, the region of a maximum Nu (Region 1, $x/d < 1.0$) and the region where Nu decreases monotonically (Region 2, $x/d > 1.0$).

In each nozzle-to-plate spacing H/d, the Nusselt number increases with the Reynolds number in all measurement points (Fig. 4). This trend has been also observed in other types of an impinging jet [5], and it is because higher jet velocity (higher Re) can convect more thermal energy from the heated plate. A more interesting trend is observed when H/d is varied at a fixed Re. As H/d increases, Nu tends to reduce in Region 1 ($x/d < 1.0$), but it shows little variation in Region 2 ($x/d > 1.0$) as demonstrated in Fig. 4.

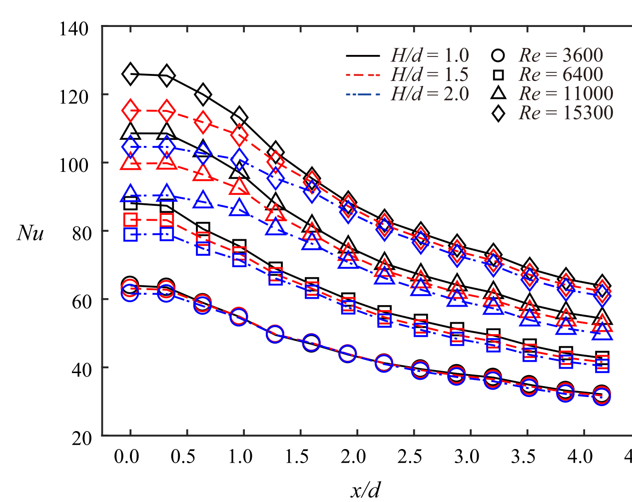

Fig. 4. Lateral variation of local Nusselt number.

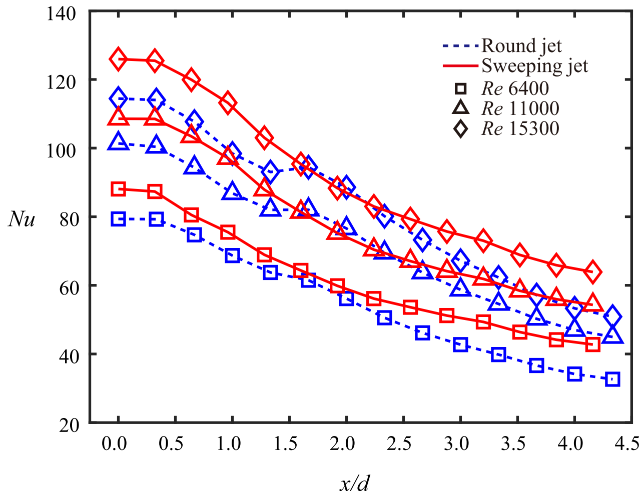

Fig. 5. Nusselt number comparison between a sweeping jet and a single steady circular jet for $H/d = 1.0$.

Compared to a steady round jet, a sweeping jet shows superior capability of heat transfer as demonstrated in Fig. 5. Additional measurement was conducted for a round jet with diameter of 6 mm. For $H/d = 1.0$, the Nusselt number of the sweeping jet is larger than that of the round jet in the measurement domain for all Reynolds numbers considered in this study. For example, at $x/d = 0$, the Nusselt number of the sweeping jet is 7–11% larger than that of the round jet. The difference in the Nusselt number between the two jets continues to reduce with lateral coordinate x/d until the point where the secondary peak of the round jet occurs and increases again thereafter. The better performance of the sweeping jet, especially near $x/d = 0$, is surprising in that the sweeping jet does not keep impinging on the center like the round jet. This result indicates that unsteady effect of the sweeping jet plays an important role in enhancing heat transfer, which will be discussed in Section 3.2.

As explained above, the sweeping jet has several noticeable trends of the heat transfer rate which have not been observed in other impinging jet types. However, from heat transfer measurement only, it is difficult to clearly understand physical mechanisms responsible for these trends; for example, why two distinct regions (Regions 1 and 2) appear and why the boundary of these regions is formed near $x/d = 1.0$. To address these questions, the flow structure of the sweeping jet will be investigated in the following section.

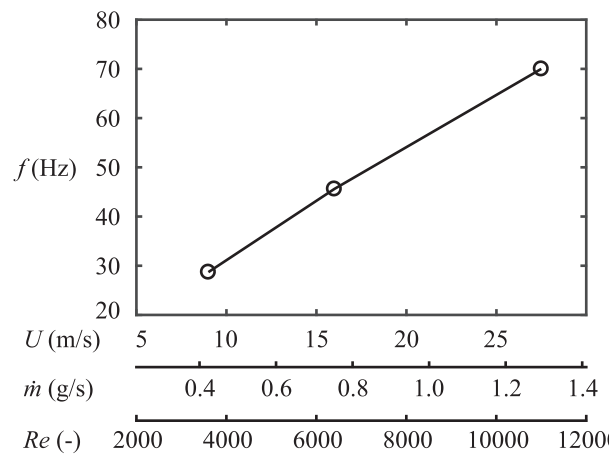

Fig. 7. Sweeping frequency of the fluidic oscillator.

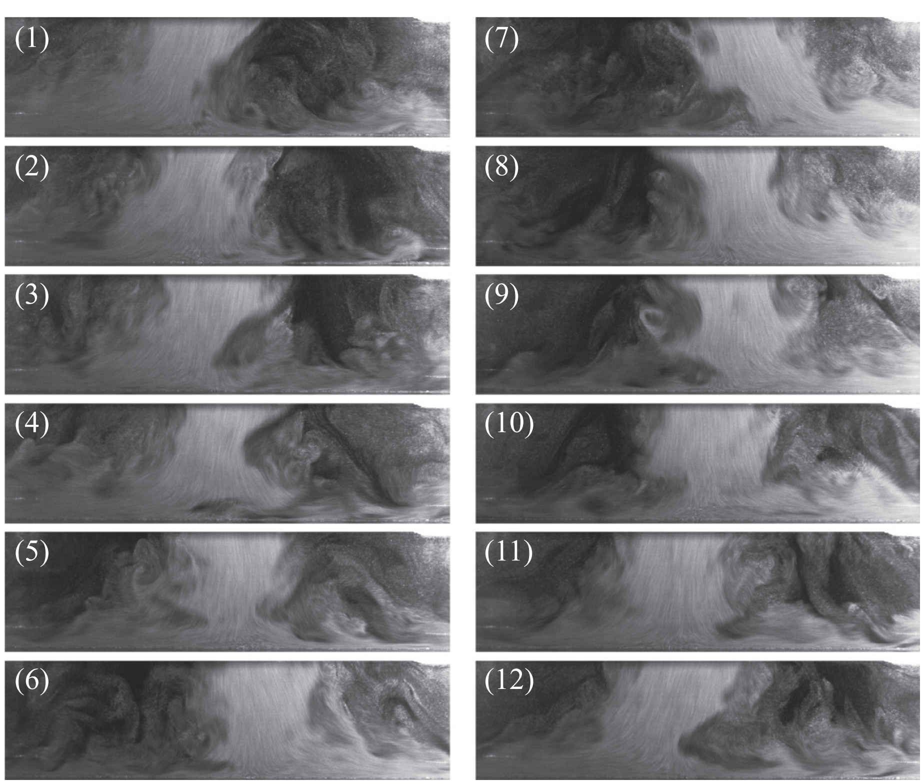

Fig. 6. Time series of a sweeping jet during one cycle ($Re = 3600$ and $H/d = 1.0$).

3.2. Flow structure of a sweeping jet

To couple heat transfer performance with flow physics, a jet flow was visualized using the PIV described in Section 2.2. Photographs in Fig. 6 show the successive stages of a sweeping jet. In Fig. 6, oil droplets ejected from the fluidic oscillator were illuminated by a laser. A primary jet from the nozzle exit moves periodically from side to side. Then, it is deflected by a wall, forming lateral wall jets on both sides of the deflection zone. The lateral wall jet in the moving direction of the primary jet is more distinct than that of the other direction. The sweeping frequency of the jet is scaled with the Reynolds number in our cases; the frequency is 28 Hz, 46 Hz, and 70 Hz for $Re = 3600$, 6400, and 11,000, respectively (Fig. 7). The sweeping frequency can be varied by the internal design and nozzle shape of the fluidic oscillator at the same Reynolds number, which changes the unsteadiness of the jet [22]. For this reason, special attention is required in conducting dimensional analysis with Re and Nu, and another dimensionless parameter including the sweeping frequency is necessary for dimensional analysis. In this study, since we use a single model of the fluidic oscillator, we will not consider the effect of such a frequency-related dimensionless parameter.

Since the sweeping jet flow is highly unsteady, little information regarding the characteristics of the jet can be obtained from the snapshots of the flow fields. Furthermore, heat transfer performance was analyzed in terms of time-averaged Nusselt number in Section 3.1. Thus, its correlation with instantaneous flow fields may lead to insubstantial conclusions. For this reason, to extract dynamic features from unsteady periodic jet motion, the POD introduced in Section 2.2 was applied.

First three POD modes, $\boldsymbol{\varphi}_1 - \boldsymbol{\varphi}_3$, are illustrated for $Re = 3600$ and $H/d = 1.0$ in Fig. 8. The first POD mode $\boldsymbol{\varphi}_1$ which represents the most dominant flow structure is shown in the form of an inclined jet (see red contours in Fig. 8(a)). Because of the periodicity of the jet, another high value of the POD mode exists in the negative x-region not mapped by PIV. In fact, the inclined shape observed in the first mode is linked to the bi-stable property of the sweeping jet. Although the jet sweeps reciprocally, it stays on both ends of the swept area for a longer time than in the middle of the swept area.

In all cases considered in this study, the first POD mode contains about 3.8–5.6% of the total kinetic energy of a fluctuating velocity component. The second and third POD modes contain about 1.4–2.8% and 0.7–1.5% of the total kinetic energy, respectively. The kinetic energy of the first POD mode is about twice larger than the second POD mode in all cases. This distribution of the relative kinetic energy indicates the dominance of the first POD mode over the rest in a sweeping jet configuration (see also Fig. 8(e)). In the case of an impinging round jet, the first POD mode is not as prevalent as the sweeping jet; the percentage of the kinetic energy is about 0.08, 0.06, and 0.05 for the first, second, and third POD modes, respectively [40].

For $H/d = 1.0$, we can identify that, along the lateral coordinate x/d near the wall, a local minimum of the first POD mode exists near $x/d = 1.0$ (Fig. 9(a)). This local minimum is formed near $x/d = 1.0$ even when nozzle-to-plate spacing changes to

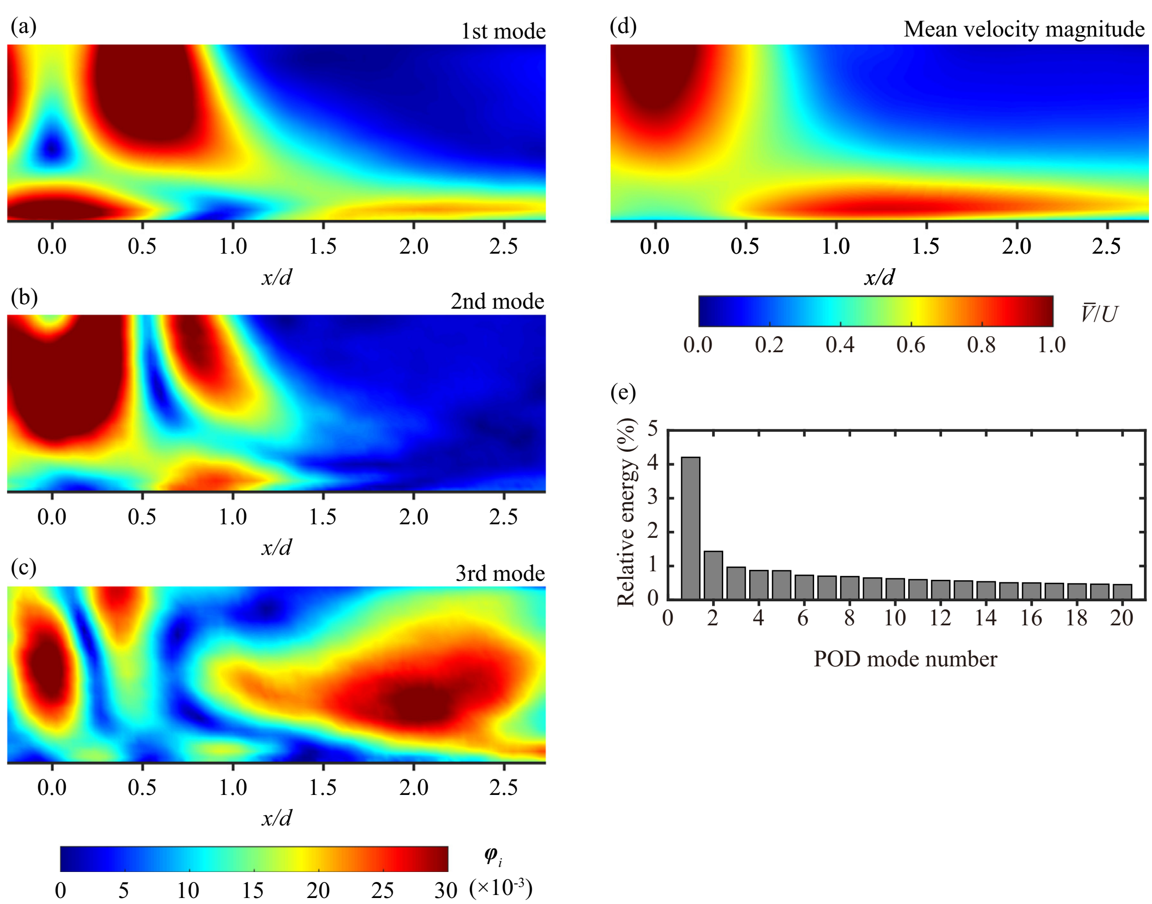

Fig. 8. Modes extracted from POD for $Re = 3600$ and $H/d = 1.0$: (a) first mode, (b) second mode, and (c) third mode. (d) Normalized time-averaged velocity magnitude $\overline{V}/U$. (e) Relative energy of the POD modes

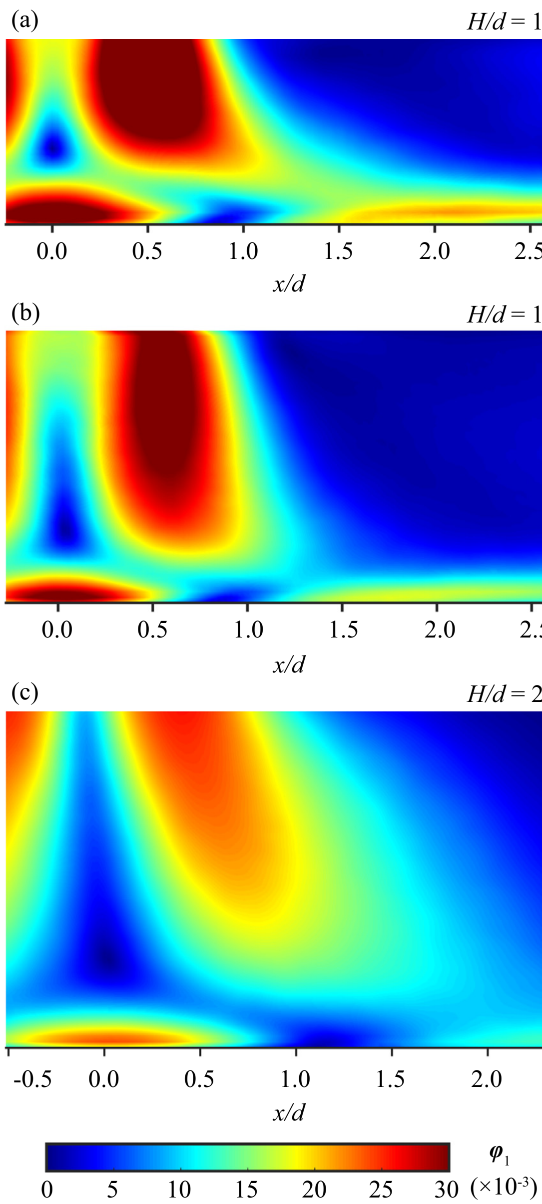

Fig. 9. First mode extracted from POD for $Re = 3600$: (a) $H/d = 1.0$, (b) $H/d = 1.5$, and (c) $H/d = 2.0$.

$H/d = 1.5$ and 2.0 (Fig. 9(b) and (c)). The local minimum of the first POD mode appears at a slightly larger lateral coordinate with increasing H/d, though. A high value of the first POD mode near the wall, in both sides of $x/d = 1.0$, is caused by the lateral wall jet deflected by the wall. We also observed that the structures of the POD modes were little affected by the Reynolds number in the range we tested. However, as the Reynolds number increases, the flow becomes more turbulent, and the relative energy of the second and third POD modes tend to be larger in comparison with that of the first POD mode.

The distribution of the first POD mode near the wall is closely related with the heat transfer performance discussed in Section 3.1. $x/d = 1$ which divides the wall into Region 1 and Region 2 in terms of heat transfer performance is actually a local minimum of the first POD mode near the wall. In addition, high Nusselt number in Region 1 is correlated with the large magnitude of the first POD mode in that region. The distribution of mean velocity magnitude $\overline{V}/U$ shows a trend strikingly different from that of the first POD mode (Fig. 8(a) and (d)). Near the wall, a region of high $\overline{V}/U$ resides between $x/d = 0.5$ and 2.0, and its value is rather smaller at the center $x/d = 0$. This trend uncorrelated with the distribution of a heat transfer rate demonstrates that heat transfer performance should be analyzed in consideration of unsteady effects rather than with time-averaged flow fields.

The dynamic features of the sweeping jet can be also inferred from the distribution of statistical quantities. In our analysis, statistical values were converged with the use of 2700 instantaneous velocity fields for each case. Non-dimensional mean lateral velocity $\bar{u}/U$ as well as maximum and minimum lateral velocities near the wall (at $y/d = 0.03$) are presented in Fig. 10. At each point of Fig. 10, the upper and lower ends of a bar indicate the maximum and minimum lateral velocities, respectively. In $x/d < 1$, the lateral flow near the wall can have negative lateral velocity and alternates its direction periodically (two-way pulsation). Mean lateral velocity $\bar{u}/U$ increases with x/d in this region. Meanwhile, in $x/d > 1$, the pulsation of the flow occurs mostly along the positive x-direction (one-way pulsation) due to the formation of a lateral wall jet, and, in contrast to $x/d < 1, \bar{u}/U$ reduces with x/d.

The RMS of velocity fluctuation is one of the statistical quantities which characterize unsteadiness of a flow. It is also called as turbulence intensity in the research of turbulent flows. Although a sweeping jet is turbulent, its velocity fluctuation is caused mainly by oscillating motion rather than by the turbulent nature of the jet itself. Thus, velocity fluctuation is considered as a more proper term than turbulence intensity in this study. The non-

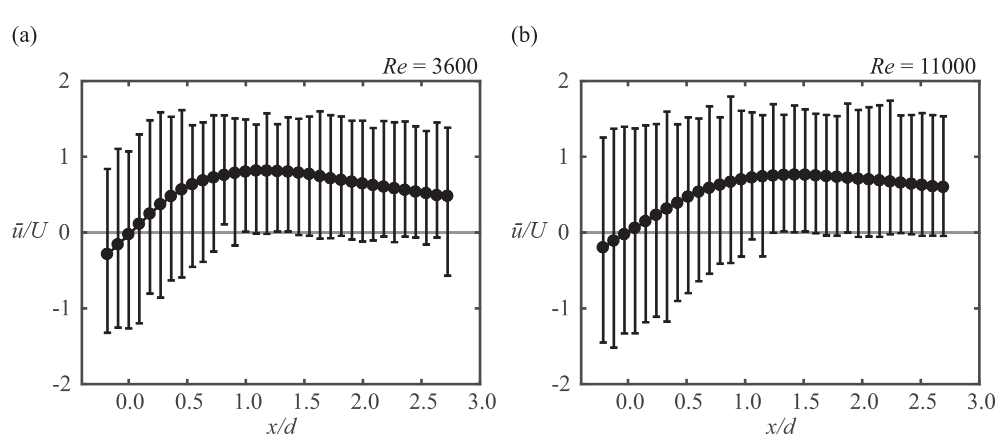

Fig. 10. Normalized time-averaged lateral velocity $\bar{u}/U$ near the wall (at $y/d = 0.03$) for $H/d = 1.0$: (a) $Re = 3600$ and (b) $Re = 11,000$.

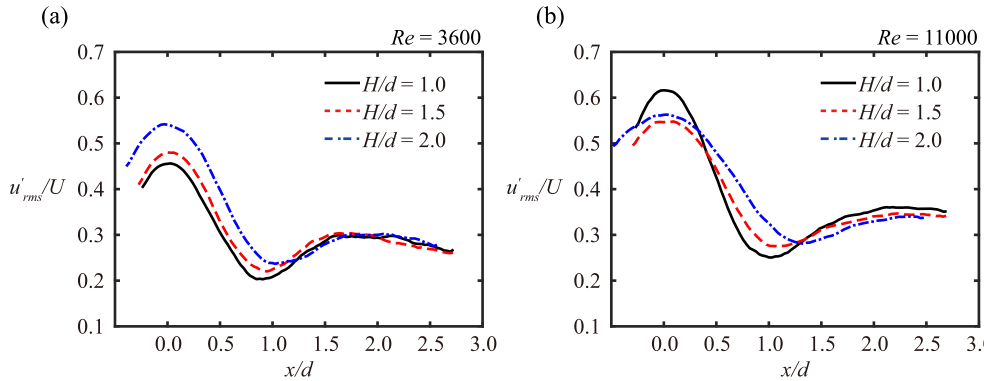

Fig. 11. Normalized RMS of the lateral velocity fluctuation u'_{rms}/U near the wall (at $y/d = 0.03$): (a) $Re = 3600$ and (b) $Re = 11,000$.

dimensional RMS of the lateral velocity fluctuation $u'_{rms}/U(=\sqrt{\overline{u'^2}}/U)$ near the wall (at $y/d = 0.03$) is plotted in Fig. 11 for $Re = 3600$ and 11,000. Lateral velocity fluctuation u'_{rms}/U near the wall is highest at the center $x/d = 0$, and its minimum appears near $x/d = 1.0$. In $x/d > 1.5$, u'_{rms}/U does not change noticeably, but exhibits a plateau instead. In a general turbulent jet, u'_{rms}/U does not exceed 0.2 at the high Reynolds number (e.g. Re=13,100) [41]. However, the peak of u'_{rms}/U stays near 0.50 for $Re = 3600$ and 0.60 for $Re = 11,000$, and even the plateau in $x/d > 1.5$ resides near 0.30 for $Re = 3600$ and 0.35 for $Re = 11,000$, which reflects the unsteadiness of the sweeping jet.

In Region 1 ($x/d < 1$), regardless of mean lateral velocity $\bar{u}/U$ smaller than that of Region 2 ($x/d > 1$), lateral velocity fluctuation u'_{rms}/U is larger because of two-way pulsation (Figs. 10 and 11). High unsteadiness in this region contributes to large Nusselt number (Fig. 4). However, our statistical approach (and POD) is not able to explicitly explain the maximum of the Nusselt number in Region 1 although we can infer that this maximum is originated by continuous sweeping motion. A further detailed analysis is required to elucidate exact cause-and-effect relation between the maximum of the Nusselt number and the sweeping motion. In Region 2 ($x/d > 1$) of one-way pulsation, $\bar{u}/U$ reduces slowly with increasing x/d whereas u'_{rms}/U stays at a nearly constant value (Figs. 10 and 11). In this aspect, heat transfer performance of Region 2, gradual decline of the Nusselt number with x/d, seems to be affected by $\bar{u}/U$ more strongly than by u'_{rms}/U.

As mentioned in Section 3.1, the maximum Nusselt number for the sweeping jet occurs at the center ($x/d = 0$) even though the sweeping jet stays on both ends of the swept area for a relatively longer time. In the sweeping jet, the velocity fluctuation representing the unsteadiness if the jet flow is rather higher in Region 1 due to the two-way pulsating wall jet. This high unsteadiness is responsible for the maximum Nusselt number near the central region. On the other hand, with the variation of H/d, the lateral velocity fluctuation is hardly changed in $x/d > 1.5$ (Fig. 11). H/d also has a negligible influence on the mean lateral velocity although not shown in this study. This trend is correlated with our finding that the Nusselt number has a similar value in Region 2 in spite of the change in H/d (Fig. 4).

As the Reynolds number (mass flow rate at the nozzle exit) increases, the sweeping frequency of the jet increases as well (Fig. 7), which causes a rise in the lateral velocity fluctuation (Fig. 11). Thus, with the current setup, it is difficult to determine whether high heat transfer performance near $x/d = 0$ in the high Reynolds number (Fig. 4) is due to solely the increasing mass flow rate or the combined effect of the increasing mass flow rate and sweeping frequency (flow unsteadiness).

4. Concluding remarks

The heat transfer of a sweeping jet impinging on a flat wall was investigated for several Reynolds numbers and nozzle-to-plate spacings experimentally. Based on the distribution of Nusselt number, the heated impingement wall can be largely divided into two regions; the Nusselt number remains high near the central region, but decreases monotonically away from the center. Heat transfer performance in these two regions were closely related with the dominant flow structure of the jet and the distribution of mean lateral velocity and lateral velocity fluctuation near the wall. We confirmed that unsteady effects caused by a sweeping motion were critical to determine a local heat transfer rate. Near the central region, the high unsteadiness of a two-way pulsation flow contributes to the increase in the heat transfer rate, which could be explained by both a high POD value and high lateral velocity fluctuation in this region. Meanwhile, in a region away from the center where a one-way pulsation flow occurs, mean lateral velocity reduces with the lateral coordinate, which is correlated with the decrease in the heat transfer rate.

As a fundamental step of applying a sweeping jet to heat transfer, we focused on finding its unique characteristics in comparison with a steady jet, instead of establishing empirical formula between Nusselt number and Reynolds number. Unsteady flow dynamics near an impingement wall and the resultant formation of an unsteady thermal boundary layer are so complicated that physical mechanisms underlying their effects on heat transfer performance still remain unclear. Thus, as a future work, the distribution of instantaneous temperature on the wall and the development of a thermal boundary layer should be taken into consideration in addition to instantaneous flow fields in order to fully understand the heat transfer performance of a sweeping jet.

Conflict of interest

None.

Acknowledgment

This research was funded by KUSTAR-KAIST Institute and the Basic Science Research Program through the National Research Foundation of Korea (NRF) funded by the Ministry of Science, ICT & Future Planning (NRF-2015R1C1A1A02037111).

References

[1] C.D. Donaldson, R.S. Snedeker, A study of free jet impingement. Part 1. Mean properties of free and impinging jets, J. Fluid Mech. 45 (1971) 281–319.

[2] C.D. Donaldson, R.S. Snedeker, D.P. Margolis, A study of free jet impingement. Part 2. Free jet turbulent structure and impingement heat transfer, J. Fluid Mech. 45 (1971) 477–512.
[3] H. Martin, Heat and mass transfer between impinging gas jets and solid surfaces, Adv. Heat Transf. 13 (1977) 1–60.
[4] S. Downs, E. James, Jet impingement heat transfer-a literature survey, in: ASME 24th National Heat Transfer Conference, 1987, pp. 1–11.
[5] K. Jambunathan, E. Lai, M. Moss, B. Button, A review of heat transfer data for single circular jet impingement, Int. J. Heat Fluid Flow 13 (1992) 106–115.
[6] D. Lytle, B.W. Webb, Air jet impingement heat transfer at low nozzle-plate spacings, Int. J. Heat Mass Transf. 37 (1994) 1687–1697.
[7] N. Zuckerman, N. Lior, Jet impingement heat transfer: physics, correlations, and numerical modeling, Adv. Heat Transf. 39 (2006) 565–631.
[8] T.S. O'Donovan, D.B. Murray, Jet impingement heat transfer–part i: mean and root-mean-square heat transfer and velocity distributions, Int. J. Heat Mass Transf. 50 (2007) 3291–3301.
[9] T.S. O'Donovan, D.B. Murray, Jet impingement heat transfer–part ii: a temporal investigation of heat transfer and local fluid velocities, Int. J. Heat Mass Transf. 50 (2007) 3302–3314.
[10] H.M. Hofmann, M. Kind, H. Martin, Measurements on steady state heat transfer and flow structure and new correlations for heat and mass transfer in submerged impinging jets, Int. J. Heat Mass Transf. 50 (2007) 3957–3965.
[11] G.M. Carlomagno, A. Ianiro, Thermo-fluid-dynamics of submerged jets impinging at short nozzle-to-plate distance: a review, Exp. Therm. Fluid Sci. 58 (2014) 15–35.
[12] J. Ferrari, N. Lior, J. Slycke, An evaluation of gas quenching of steel rings by multiple-jet impingement, J. Mater. Process. Tech. 136 (2003) 190–201.
[13] N.D. Francis, W.J. Wepfer, Jet impingement drying of a moist porous solid, Int. J. Heat Mass Transf. 39 (1996) 1911–1923.
[14] A. Pavlova, M. Amitay, Electronic cooling using synthetic jet impingement, J. Heat Transf. 128 (2006) 897–907.
[15] J.C. Han, Recent studies in turbine blade cooling, Int. J. Rotating Mach. 10 (2004) 443–457.
[16] K.S. Choo, S.J. Kim, Comparison of thermal characteristics of confined and unconfined impinging jets, Int. J. Heat Mass Transf. 53 (2010) 3366–3371.
[17] X.M. Tan, J.Z. Zhang, Flow and heat transfer characteristics under synthetic jets impingement driven by piezoelectric actuator, Exp. Therm. Fluid Sci. 48 (2013) 134–146.
[18] D. Trainer, J. Kim, S.J. Kim, Heat transfer and flow characteristics of air-assisted impinging water jets, Int. J. Heat Mass Transf. 64 (2013) 501–513.
[19] V. Terekhov, S. Kalinina, K. Sharov, An experimental investigation of flow structure and heat transfer in an impinging annular jet, Int. Commun. Heat Mass Transf. 79 (2016) 89–97.
[20] S. Raghu, Fluidic oscillators for flow control, Exp. Fluids 54 (2013) 1455.
[21] L.N. Cattafesta III, M. Sheplak, Actuators for active flow control, Annu. Rev. Fluid Mech. 43 (2011) 247–272.
[22] J.W. Gregory, M.N. Tomac, A review of fluidic oscillator development and application for flow control, in: 43rd Fluid Dynamics Conference, 2013, p. 2474.
[23] G. Raman, S. Raghu, Cavity resonance suppression using miniature fluidic oscillators, AIAA J. 42 (2004) 2608–2612.
[24] G. Raman, S. Packiarajan, G. Papadopoulos, C. Weissman, S. Raghu, Jet thrust vectoring using a miniature fluidic oscillator, Aeronaut. J. 109 (2005) 129–138.
[25] W.B. Zimmerman, B.N. Hewakandamby, V. Tesař, H.H. Bandulasena, O.A. Omotowa, On the design and simulation of an airlift loop bioreactor with microbubble generation by fluidic oscillation, Food Bioprod. Process. 87 (2009) 215–227.
[26] R. Seele, E. Graff, M. Gharib, L. Taubert, J. Lin, I. Wygnanski, Improving rudder effectiveness with sweeping jet actuators, in: 6th AIAA Flow Control Conference, 2012, p. 3244.
[27] B.J. Slupski, K. Kara, Separated flow control over NACA 0015 airfoil using sweeping jet actuator, in: 35th AIAA Applied Aerodynamics Conference, 2017, p. 3044.
[28] D. Thurman, P. Poinsatte, A. Ameri, D. Culley, S. Raghu, V. Shyam, Investigation of spiral and sweeping holes, J. Turbomach. 138 (2016) 091007.
[29] M.A. Hossain, R. Prenter, R.K. Lundgreen, L.M. Agricola, A. Ameri, J.W. Gregory, J.P. Bons, Investigation of crossflow interaction of an oscillating jet, in: 55th AIAA Aerospace Sciences Meeting, 2017a, p. 1690.
[30] M.A. Hossain, R. Prenter, R.K. Lundgreen, A. Ameri, J.W. Gregory, J.P. Bons, Experimental and numerical investigation of sweeping jet film cooling, in: ASME Turbo Expo, 2017b, p. 64479.
[31] R.K. Lundgreen, M.A. Hossain, R. Prenter, J.P. Bons, J. Gregory, A. Ameri, Impingement heat transfer characteristics of a sweeping jet, in: 55th AIAA Aerospace Sciences Meeting, 2017, p. 1535.
[32] R.D. Stouffer, Oscillating Spray Device, 1979. US Patent 4,151,955.
[33] S. Caliskan, S. Baskaya, Experimental investigation of impinging jet array heat transfer from a surface with v-shaped and convergent-divergent ribs, Int. J. Heat Mass Transf. 59 (2012) 234–246.
[34] R.J. Goldstein, E.M. Sparrow, D.C. Jones, Natural convection mass transfer adjacent to horizontal plates, Int. J. Heat Mass Transf. 16 (1973) 1025–1035.
[35] S.W. Churchill, H.H.S. Chu, Correlating equations for laminar and turbulent free convection from a vertical plate, Int. J. Heat Mass Transf. 18 (1975) 1323–1329.
[36] R.J. Goldstein, K.S. Lau, Laminar natural convection from a horizontal plate and the influence of plate-edge extensions, J. Fluid Mech. 129 (1983) 55–75.
[37] L. Sirovich, Turbulence and the dynamics of coherent structures, Q. Appl. Math. 45 (1987) 561–571.
[38] G. Berkooz, P. Holmes, J.L. Lumley, The proper orthogonal decomposition in the analysis of turbulent flows, Annu. Rev. Fluid Mech. 25 (1993) 539–575.
[39] P. Holmes, Turbulence, Coherent Structures, Dynamical Systems and Symmetry, Cambridge University Press, 2012.
[40] K.J. Hammad, I.M. Milanovic, A POD study of an impinging jet flow field, in: ASME Fluids Engineering Division Summer Meeting, 2009, pp. 2–6.
[41] K. Nishino, M. Samada, K. Kasuya, K. Torii, Turbulence statistics in the stagnation region of an axisymmetric impinging jet flow, Int. J. Heat Fluid Flow 17 (1996) 193–201.